Batteries & Supercaps

Research Article
doi.org/10.1002/batt.202200087

Chemistry Europe
European Chemical
Societies Publishing

www.batteries-supercaps.org

Self-Generated Template Assisted Construction of Nitrogen Self-Doped Porous Carbon Nanoframework with Rich Planar Holes for High Energy Density Supercapacitor

Shengliang Qi+,[a] Xin Wang+,[a] Jia Kang,[a] Yangfei Hu,[a] Nan Xu,[a] Mengna Zhang,[a] Hui Peng,*[a] and Guofu Ma*[a]

Nitrogen-doped porous carbon materials with planar holes not only inherit the structure advantages of porous carbon materials, but also have a unique planar porosity and heteroatomic doping feature, showing enormous interest in the field of energy storage and conversion. Nevertheless, rational and controllable design of honeycomb-like porous carbon materials with rich planar holes remains a tremendous challenge. Herein, we develop a "bottom-up" self-assembly of carbon- and nitrogen-rich conjugated polymer and subsequent potassium ferrate (K_2FeO_4) facilitated activation, catalysis and self-generated template assisted carbonization strategy to construct nitrogen self-doped honeycomb-like porous carbon nanoframework (NHPC) with rich planar holes. By exploiting the advantages of the integral and interconnected honeycomb-like carbon skeleton and rich planar holes (rapid ion/electron diffusion) and the efficient nitrogen doping (improved wettability), the NHPC possesses high specific capacitance of 288 F g^{-1} at 0.5 A g^{-1} and outstanding rate performance. In addition, an aqueous symmetric supercapacitor fabricated from NHPC electrodes possesses widened potential window of 2.0 V, high energy density of 23.6 Wh kg^{-1} at 500 W kg^{-1}, as well as excellent electrochemical stability (91.2% capacitance retention after 20,000 cycles).

Introduction

Two-dimensional (2D) materials exhibit fascinating physical and chemical properties due to their high surface-to-volume ratios and surface charge.[1,2] In particular, 2D carbon nanosheets have received extensive attention in advanced catalysis and energy storage/conversion as a result of their unique structures, high intrinsic electrical conductivity, tunable surface chemistry, low mass density and/or interconnected pore structure at different length scales, excellent mechanical/chemical stability and so on.[3–5] Furthermore, carbon superstructures consisting of hierarchical pores (micro-, meso-, and macro-pores), especially the suitable planar holes on the 2D sheets, not only exhibit high specific surface area and porosity, but also boost the permeability of mass/ions on the surface and internal space of carbon skeleton, thereby improving electrochemical performance and expanding its application in various fields.[6,7] Therefore, the strategies to simultaneously combine the superiorities of 2D features and unique hierarchical pores architectures are being sought in carbon materials recently.[4] It was reported that carbon superstructures deliver ultra-stable charge storage and fast proton-coupled kinetics at the structural-chemical defects for efficient energy storage.[8]

The "top-down" approach including chemical/electrochemical exfoliation or mechanical cutting has been widely introduced to develop carbon superstructures,[9,10] and subsequent use strong alkali (KOH)/oxidant (H_2O_2) chemicals to etch carbon skeleton to generate nanopores and/or planar holes structures.[11–14] However, the "top-down" strategy for preparing carbon nanosheets have more or less deficiencies, such as low yield, complicated experimental procedures and poor reproducibility.[15] Moreover, the structure, size, density, and site of the generated pores in carbon nanosheets may be difficult to control precisely by strong alkali/oxidant etching.[16] Holey carbon nanosheets prepared by external alkaline metal-assisted pyrolysis of natural biomass can effectively increase the yield, but the resulting structure is severely restricted by the intrinsic microstructure of the precursor, and the pores and holes in the carbon skeleton are usually fails to properly controlled.[15] Therefore, it is well worth exploring an economic, controllable and scalable synthesis strategy for carbon skeleton with planar holes, which involve the starting materials with designable, adjustable microstructures and use mild and versatile chemicals.

In recent years, 2D/3D conjugated polymers with special architecture were subtly regulated and synthesized through a "bottom-up" self-assembly crystal growth process under mild conditions.[17–20] Particularly, those conjugated polymers with aromatic amides skeletons are ideal alternative precursors for the template-free fabrication of carbon superstructures, because of their carbon- and nitrogen-rich conjugated frame-

works, inherent high thermal stability, and the morphology and microstructure of conjugated polymers can be regulated and controlled flexibly through well-orchestrated selecting polymeric monomers and tuning the crystal growth parameters.[14,21–24] However, direct pyrolysis of these precursors in the absence of activation treatment is often hard to achieve carbon material with high porosity, especially carbon skeleton with planar holes, although the intrinsic morphology can be retained.[16,25] Traditional activating reagents such as $ZnCl_2$, KOH and $KHCO_3$ have long been proved to greatly improve the pore structure of carbon materials, but the shape/size distribution of the generated pores is uncontrolled and irregular, and it is even more difficult to generate regular planar holes.[26–28] For this reason, it is very necessary to seek an environmentally friendly, mild and multifunctional activating reagent to simultaneously realize the flourishing pore structure and enhanced graphitization of carbon materials, yet inducing the formation of planar holes in carbon skeleton.

Here we demonstrate a novel strategy to produce nitrogen self-doped honeycomb-like porous carbon nanoframework (NHPC) with rich planar holes for ultra-stable energy storage by using carbon- and nitrogen-rich conjugated polyimide as precursor and potassium ferrate (K_2FeO_4) as multifunctional carbonization reagent. In which, the K_2FeO_4 plays the multiple roles of activating agent, catalyst and self-generated template precursor during high temperature pyrolysis process, because it is thermally decomposed to produce potassium carbonate (K_2CO_3), iron oxide (Fe_2O_3) and iron nitride (Fe_3N). The activation mechanism of K_2FeO_4 was carefully analyzed, and the influences of different carbonization temperatures on pore structure characteristics, density of planar holes, nitrogen doping amount and electrochemical properties of NHPC were systematically investigated. The optimized NHPC achieves high specific surface area, high specific capacitance and excellent rate capability. More importantly, the symmetric supercapacitor fabricated based on NHPC electrode has a wide operating voltage of 2.0 V and high specific energy and long-term lifespan in aqueous electrolyte.

Results and Discussion

Nitrogen self-doped honeycomb-like porous carbon nanoframework (NHPC) with rich planar holes is prepared by potassium ferrate (K_2FeO_4) facilitated activation, catalysis and self-generated template assisted high temperature carbonization and acid etching treatment process using polymerized polyimide (PI) microspheres as carbon precursor, as shown in Scheme 1. First, the PI microspheres composed of intertwined and vertical nanosheets (Figure S1) were synthesized by low-temperature self-assembly polymer crystallization process from binary anhydride (BTDA) and diamine (EDA) monomers. For "bottom-up" self-assembly process of PI from polyamic acid (PAA), the crystallization of PI involves the folding back and forth of one-dimensional polymer chains, the assembly of chains into two-dimensional lamellar structures, and the further assembly of sheets into three-dimensional spherical crystalline structures.[29] The PI microspheres with typical aromatic amide skeleton exhibit good thermal stability and rich in nitrogen species, which provides an ideal carbon precursor for preparing nitrogen self-doped porous carbon materials with an integral superstructure.[23] Second, to obtain high porosity and precisely controlled carbon materials with rich planar holes, the potassium ferrate (K_2FeO_4) was selected and used as the multiple roles of activating agent, catalyst and self-generated template precursor during high temperature pyrolysis process, because it is thermally decomposed to produce potassium carbonate (K_2CO_3), iron oxide (Fe_2O_3) and iron nitride (Fe_3N).[30]

As shown in Figure 1a, it can be found that there are different metallic compounds substances in carbon materials will be generated at different pyrolysis temperatures with K_2FeO_4 assisted activation before etching with acid. In detail, X-ray powder diffraction (XRD) results suggest that the main decomposition results in the formation of a mixture of K_2CO_3 and Fe_2O_3 as the temperature promoted to 500 °C. The related reactions can be expressed as follows: (1) $4 K_2FeO_4 = 2 Fe_2O_3 + 3 O_2 + 4 K_2O$; (2) $K_2O + CO_2 = K_2CO_3$.[26,28] When the temperature reaches 600 °C or higher (700 °C), it mainly decomposes to form
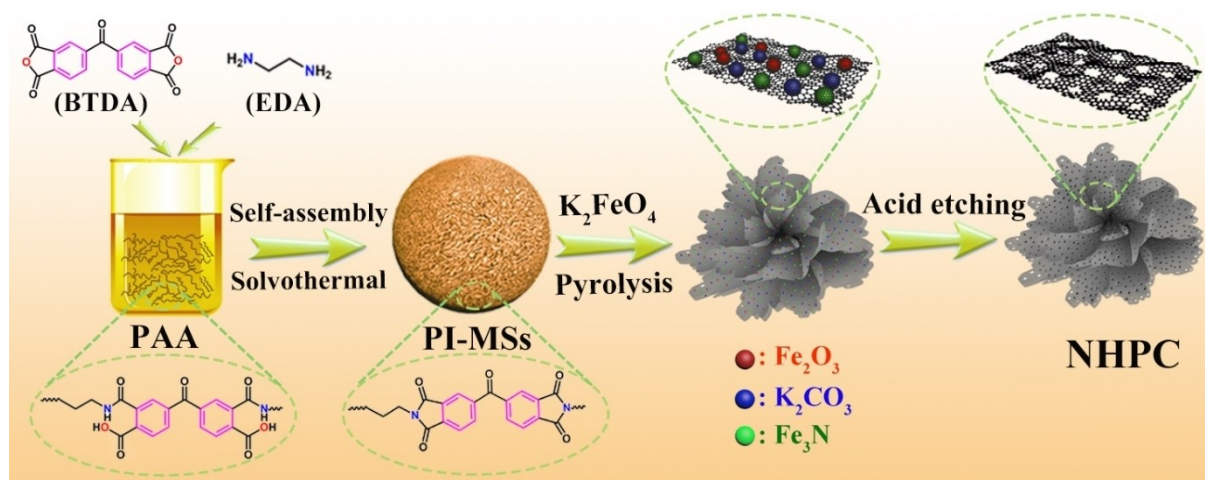
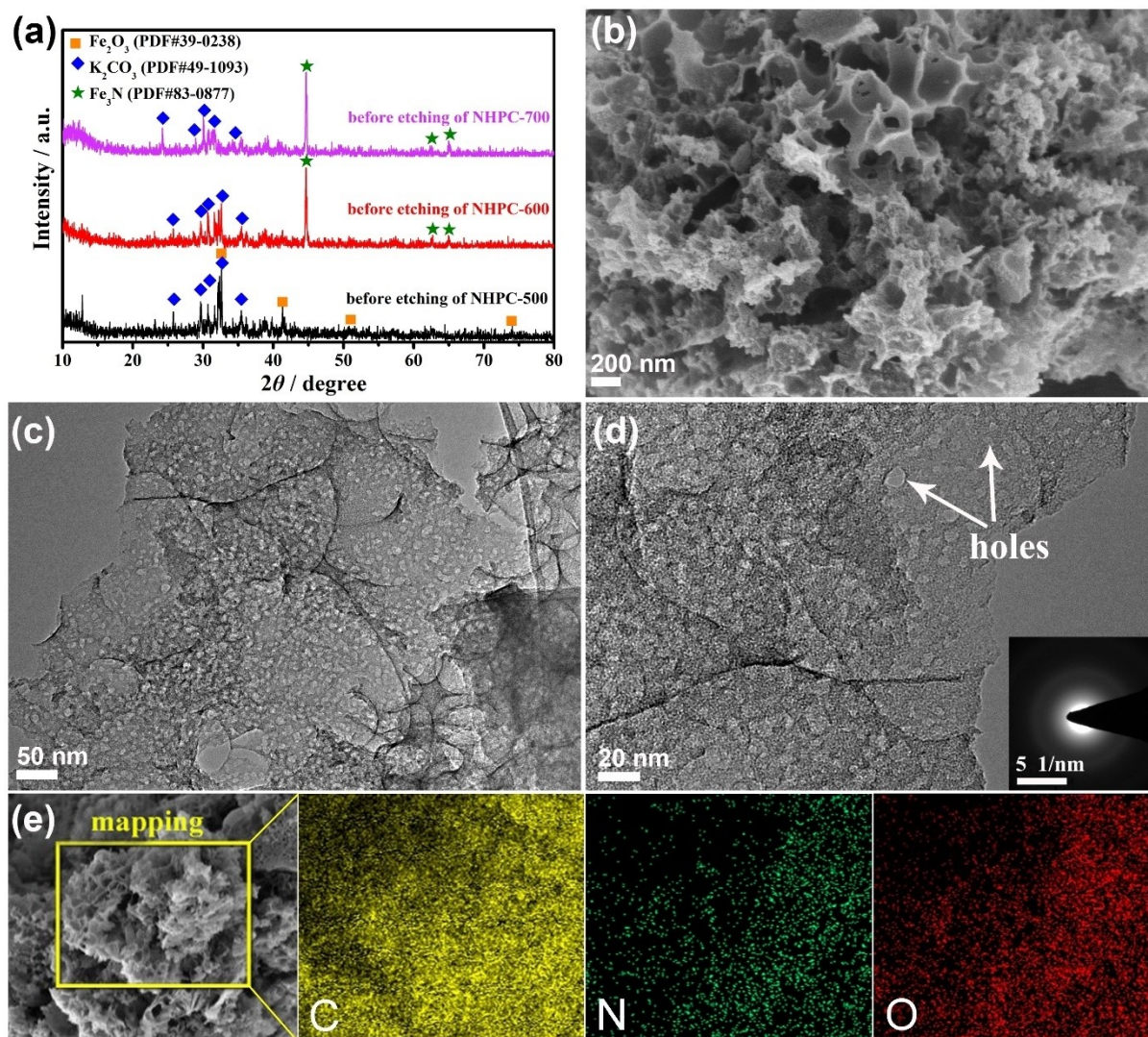**Scheme 1.** Illustration of the fabrication process of NHPC.

Figure 1. a) XRD patterns of the NHPC materials before acid etching; b) SEM image of the NHPC-600; c and d) TEM images of NHPC-600; e) EDS elemental mapping images of the NHPC-600.

a mixture of K_2CO_3 and Fe_3N, while the initial Fe_2O_3 disappears. This is because the Fe_2O_3 was further in-situ reduced by carbon to Fe nanoparticles, and then immediately react with nitrogen-reductive species originated from the thermal decomposition of PI to generate iron nitride (Fe_3N).[31] The thermally decomposed to produce K_2CO_3, Fe_2O_3 and Fe_3N can be used as the activator, catalyst and pore forming template during high temperature pyrolysis of PI microspheres to generate well-developed pore structures,[32] respectively. Previous studies have found that K_2CO_3 activation involved the reduction of K_2CO_3 to metallic potassium/potassium compounds (K/K_2O) and expanding gases (CO and CO_2) during the activation process.[33] Thus, the gasification expansion can promote the formation of honeycomb-like porous carbon nanoframework, while the potassium species and iron compounds infiltrate into the internal structure of the carbon matrix can enhance the existing pores and generates new porosities. In addition, non-volatile metal compounds (Fe_2O_3 and Fe_3N) can be embedded into

carbon skeleton at high temperature as in situ self-generating templates, and the honeycomb-like porous carbon nanoframework with rich planar holes can be obtained after removing the metal compounds by acid etching.

It can be seen from the scanning electron microscopy (SEM) images of PI that the it appears as a microsphere with a diameter of about 10 μm (Figure S1a and b) and surface of PI microspheres is composed of intertwined and vertical nanosheets subunits (Figure S1c and d). While the honeycomb-like porous carbon nanoframework morphology can be found from NHPC-600 when the PI microspheres were activated and catalytic carbonized by K_2FeO_4 (Figure 1b). Similarly, both NHPC-500 (Figure S2a and b) and NHPC-700 (Figure S2d and e) materials prepared at carbonization temperatures of 500 °C and 700 °C are also exhibit honeycomb-like porous nanofoam structures. However, the morphology of PI-600 without K_2FeO_4 activation treatment shows irregularly agminated microspheres with dense cracks surface (Figure S2g and h), which may be

Batteries & Supercaps

Research Article
doi.org/10.1002/batt.202200087

Chemistry Europe
European Chemical
Societies Publishing

due to the volume shrinkage of polymer microspheres and the escape of volatile small molecules during high temperature pyrolysis.[34] These results indicate that K_2FeO_4-assisted activation can promote the formation of honeycomb-like porous carbon nanoframework, which involves potassium and/or iron compounds activation and gasification expansion processes.[31,33] Considering the NHPC-600 material delivers the best chemical capacitive energy storage among those materials, we thus take it as the typical example for further structural and morphological investigations.

The microstructure of typical porous carbon nanoframework (NHPC-600) was further characterized by transmission electron microscopy (TEM). More shockingly, the highly folded layered ultrathin nanosheets with lush and unified planar holes are expressly found from the high magnification images (Figure 1c). Such unparalleled structure was exceedingly conducive to the penetration and diffusion of electrolyte ions, and thus consumedly enhancing the electrochemical performance of the porous carbon materials.[11,35] Distinctively, NHPC-600 material before acid etching showed dense and fine nanoparticles embedded in the carbon nanoframework (Figure S3a), and no obvious planar holes were observed (Figure S3c).The high resolution TEM image further confirmed that a large number of planar holes with diameter of 3–9 nm are decorated in the carbon skeleton of NHPC-600 (Figures 1d and S4). In addition, the energy dispersive spectra (EDS) element mapping revealed that the C, N and O elements are uniformly distributed in NHPC series and PI-600 materials (Figures 1e and S2), signifying effective nitrogen doping in PI-derived carbon matrix. Moreover, NHPC-500 material exhibits overlapping carbon nanoframework morphology decorated with sparse and cluttered planar holes (Figure S5a), while the NHPC-700 exhibits honeycomb-like carbon nanoframework with dense planar holes (Figure S5b). According to the TEM results, the following rules can be found that the number of planar holes in carbon skeleton is greater as the carbonization temperature increases (Figures 1c and S5). However, the PI-600 without K_2FeO_4 activation showed unbroken carbon microspheres (Figure S5c), and the edges of the microspheres have no interwoven nanosheet structure and obvious holes (Figure S5d). By comparison, the NHPC-600 material not only has an integral and interconnected porous carbon nanoframework, but also the planar holes of the carbon skeleton are evenly inlaid, which can provide fast electron transmission paths and electrolyte ion penetration channels.

The specific surface area and porosity of all carbon materials were studied by the Brunauer-Emmett-Teller (BET) method and their results are shown in the Figure 2(a). It can be found that the PI-600 material without K_2FeO_4 activation treatment exhibits a Type-I isotherm and has a low adsorption/desorption volume. In comparison, all the NHPC materials exhibit type-IV isotherm characteristics, which comprising of adsorption regions in the low relative pressure ($P/P_0 < 0.1$) and well-defined plateaus with distinctive hysteresis loops ($P/P_0 = 0.45–0.90$), intimating the presence of abundant micro- and mesopores.[36] The specific surface area and pore structure parameters of NHPC series and PI-600 materials are listed in

Table S1. One can see that the specific surface area of NHPC increases with carbonization temperature increasing, demonstrating that the enhanced temperature could effectively promote the activation ability.[37] Specifically, the specific surface area of NHPC-500, NHPC-600 and NHPC-700 is 657.6 $m^2 g^{-1}$, 971.5 $m^2 g^{-1}$ and 1054.4 $m^2 g^{-1}$, respectively. Besides, the specific surface area of NHPC-600 is much higher than the PI-600 material (58.9 $m^2 g^{-1}$) at the same pyrolysis temperature, which proves that K_2FeO_4 activation treatment can obviously enhance the porosity of carbon materials. In addition, the pore size distribution results show that the pore size range of NHPC materials is mainly concentrated in 3–6 nm, indicating that they have a typical mesoporous structure, which is critical for improving the electrochemical energy storage performance of carbon materials in aqueous electrolytes.[38] The pore size of some mesoporous is also consistent with TEM images of planar holes decorated in the carbon skeleton of NHPC-600. In addition, the results of element analysis further confirmed the effective nitrogen self-doping in NHPC series and PI-600 materials (Table S1), which is derived from the aromatic amide skeleton of PI precursor. As the pyrolysis temperature increased from 500 °C to 700 °C, the nitrogen content of the carbon materials decreased from 3.2 wt% to 0.4 wt%, which was attributed to the evaporation of nitrogen atoms at high pyrolysis temperature.[34]

Figure 2(c) revealed the XRD patterns of NHPC and PI-600 materials. Different from the strong diffraction peaks of PI, both NHPC and PI-600 have broad and weak diffraction peaks, insinuating that these materials are primarily comprised of amorphous carbon skeleton. Two relatively sharp diffraction peaks appeared at approximately 25° and 44° are indexed to the (002) and (101) crystal planes of graphitic carbon, respectively. It can be seen that the typical (002) crystal plane of NHPC shift to a higher 2θ degree with the increase of pyrolysis temperature (Figure 2c). According to the Bragg's law ($2d\sin\theta = n\lambda$), the increase of diffraction angle signifies the decrease of interlayer spacing originated from the increase of the stacking degree of the graphite layer with increase in carbon content at high pyrolysis temperature.[39] These defect and graphitized structure are further studied by Raman spectroscopy (Figure 2d). The D-band at 1347 cm^{-1} and G-band at 1589 cm^{-1} are homologous to the defect of carbon layer and the vibration of sp2 planar carbon phase, respectively. The intensity ratio of I_D/I_G increase from 0.82 to 0.92 as the pyrolysis temperature enhanced, which is due to the synergistic effect of disordered structure and graphitization,[40] in consistent with XRD characterization. The X-ray photoelectron spectroscopy (XPS) was employed to further analyze the composition and chemical state of the surface chemical elements in NHPC-600 material (Figure 2e and f). The full XPS spectrum demonstrates the C, O and N elements in NHPC-600 material and their content is 88.6%, 9.4% and 2.0%, respectively. The N content is extremely similar to that of element analysis results in Table S1. Moreover, the high-resolution N 1s spectrum (Figure 2f) can be fitted into four types of peaks: pyridinic N (398.4 ± 0.2 eV), pyrrolic N (400.0 ± 0.2 eV), graphitic N (400.9 ± 0.2 eV) and pyridinic N^+-O^- (402.6 ± 0.3 eV).[41] It was suggested that

Batteries & Supercaps

Research Article
doi.org/10.1002/batt.202200087

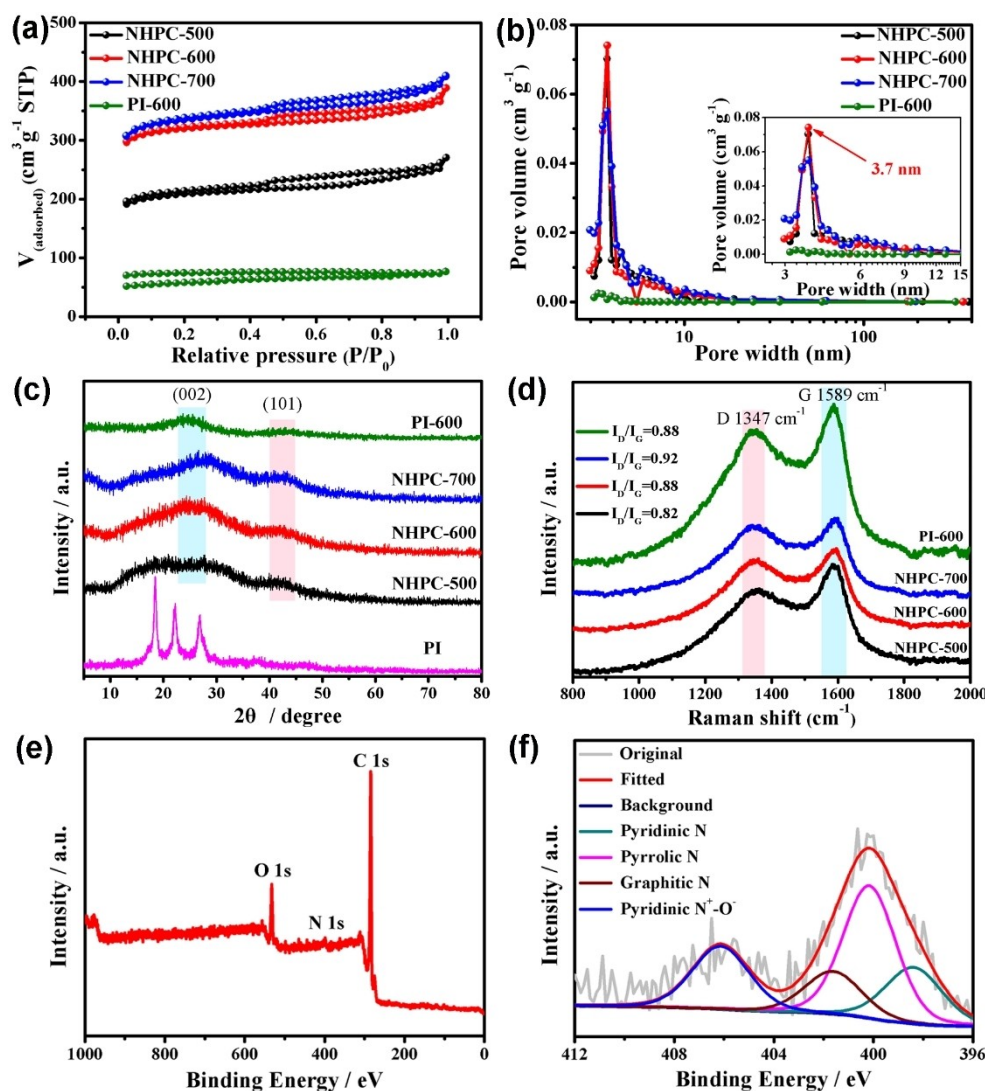**Chemistry Europe**
European Chemical
Societies Publishing

Figure 2. a) Nitrogen adsorption-desorption isotherms and b) pore size distribution curves of NHPC and PI-600; c) XRD patterns of NHPC and PI-600, d) Raman spectra of NHPC and PI-600; e) survey XPS spectrum and f) high-resolution N1s spectrum of NHPC-600.

presence of pyridinic N and pyrrolic N in carbon skeleton can promote the specific capacitance of carbon materials, while graphitic N and pyridinic N^+-O^- can boost the conductivity and electron transfer.[42] As evidenced in Figure 2(f), the proportion of pyrrolic N and pyridinic N^+-O^- in NHPC-600 material is higher than that of other types of nitrogen, indicating it has synergistic capacitive energy storage and high electron transfer capability.

The honeycomb-like porous carbon nanoframework morphology, abundant mesoporous and planar holes, effective nitrogen doping and high graphitized structure may endow the NHPC materials with efficient ion/electron diffusion and improved wettability when used as electrode material in supercapacitor, thus it is expected to obtain excellent electrochemical performance. To investigate the electrochemical behavior of NHPC and PI-600, cyclic voltammetry (CV) and galvanostatic charge and discharge (GCD) curves were determined in 2 M KOH aqueous electrolyte employing a three-

electrode system. As shown in Figure 3(a), the CV profiles of all the NHPC materials emerge rectangular-like shape, presenting double-quick electrochemical response and emphasizing electric double-layer capacitor characteristic. In contrast, PI-600 exhibits a small and irregular triangular curve from low potential to high potential, which is originated from the blocked diffusion of electrolyte ions and thus lead to an ion sieving effect,[43] resulting in low charge response and migration rate. The integral area of CV curve intimated the specific capacitance of electrode materials, which related to ion adsorption capacity of carbon materials. Obviously, the CV integral area of the typical NHPC-600 electrode is largest among the four carbon materials, revealing the most prominent specific capacitance. The CV curves of NHPC-600 electrode at different scan rates are shown in Figure 3(b). The NHPC-600 electrode exhibits outstanding capacitive behavior with a rectangle-like shape even at high scan rate of 100 mV s^{-1}.
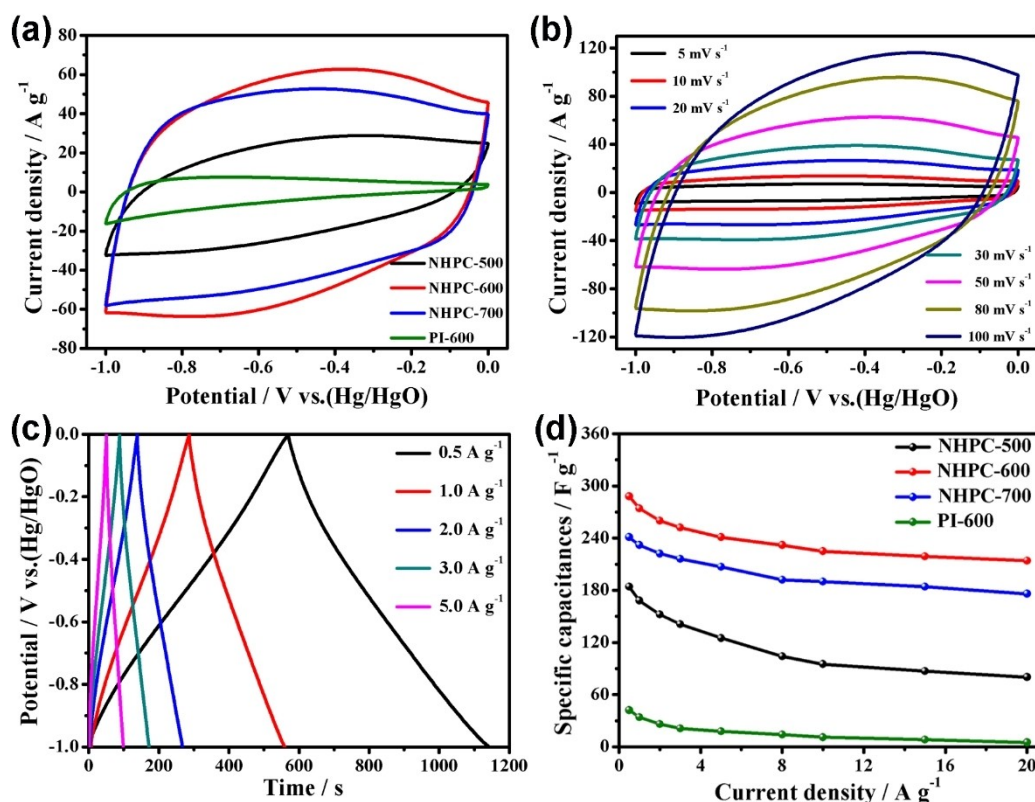
Figure 3. a) CV curves of NHPC and PI-600 at 50 mV s^{-1}; b) CV curves of NHPC-600 at various scan rates; c) GCD curves of NHPC-600 at different current densities; d) specific capacitances of NHPC and PI-600 materials at different current densities.

It can be seen from Figure 3(c) that the GCD curves of NHPC-600 electrode show ideal symmetrical isosceles triangle at various current densities, demonstrating highly reversible double-layer capacitive behavior. Moreover, NHPC-600 electrode possesses a high capacitance of 288 F g^{-1} at 0.5 A g^{-1} and remains above 74% original capacitance even at high current density up to 20 A g^{-1}, which value is larger than that of NHPC-500 and NHPC-700 materials, and much larger than PI-600 material (Figure 3d). The volumetric capacitance of the electrode material also shows that the NHPC-600 material has the highest capacity and rate performance among these materials (Figure S6). Electrochemical impedance spectroscopy (EIS) measured were performed to further evaluate the electrochemical properties of carbon materials (Figure S7a). The NHPC-600 electrode possesses a small internal series resistance (Rs) and charge transfer resistance (R_{ct}) compared to other carbon materials, because it has a small real axis (Z') intercept and semicircle in the high frequency region].[44] According to the Nyquist plots of NHPC, the electrical conductivity of NHPC-500, NHPC-600 and NHPC-700 is 0.64 S m^{-1}, 1.07 S m^{-1} and 0.95 S m^{-1} (Table S1), respectively. It can be found that the electrical conductivity of NHPC materials shows an increasing trend with the increase of carbonization temperature, indicating that increasing carbonization temperature can effectively improve its graphitization degree and thus improve the conductivity. In addition, the conductivity of NHPC-600 is slightly higher than that of NHPC-700, which is due to the high

nitrogen doping content of NHPC-600. Furthermore, diffusion coefficient (D) of the ions across the electrode/electrolyte interface is calculated from the slope of plot Z vs. $\omega^{1/2}$ (Figure S7b). The high D value of NHPC-600 is attributed to the high electrical conductivity and rich charged surface (high nitrogen content) of carbon materials. The order of magnitude of the D was 10^{-5} cm^2 s^{-1}, in good agreement with the fast response and high rate performance of the carbon materials. The NHPC-600 electrode has outstanding cycling stability with 95.45% of the capacitance retention after 20,000 cycles (Figure S8). The excellent electrochemical properties of NHPC-600 material can be attributed to combination of integral and interconnected porous carbon nanoframework structure, abundant and uniform planar holes in carbon skeleton, and high nitrogen doping content, which provide fast electron transmission paths and electrolyte ion penetration channels,[45] thereby deliver high conductivity, high charge storage capacity and excellent rate performance.

To further estimate the actual electrochemical performance of typical NHPC-600 material, the symmetric supercapacitor device is fabricated by using NHPC-600 as electrode material in 2 M KOH electrolyte. The electrochemical properties of the symmetric supercapacitor are shown in Figure S9. The operating voltage of the symmetric supercapacitor assembled with 2 M KOH aqueous electrolyte is only 1.0 V, resulting in its energy density of only 5.07 Wh kg^{-1} at a power density of 250 W kg^{-1}. Recent studies have confirmed that the neutral

Batteries & Supercaps

Research Article
doi.org/10.1002/batt.202200087

Chemistry Europe
European Chemical
Societies Publishing

aqueous electrolyte can be delivered a wider operating voltage than acid and alkali aqueous electrolyte because of their lower concentration of hydrogen ion or hydroxide ion.[38] Thus, the symmetric supercapacitor device based on NHPC-600 material was fabricated in 0.5 M Na_2SO_4 aqueous electrolyte in this work. To ensure the electrochemical stability and reasonably select the actual operating voltage of the device, the CV curves of the device in the potential range of 1.0 to 2.0 V was first measured, as shown in Figure 4(a). It can be found that the symmetric supercapacitor device can maintain a stable rectangular-like shape even at a high operating voltage of 2.0 V without hydrogen/oxygen evolution. Therefore, the voltage of 2.0 V can be selected as the operating voltage of the device for subsequent electrochemical performance tests.

Figure 4b exhibited the CV curves of symmetric supercapacitor at various scan rates, showing rectangular-like shapes

of ideal capacitive behavior. Besides, corresponding symmetrical triangle shapes can be observed from the every GCD curves of symmetric supercapacitor at various current densities (Figure 4c), demonstrating that it possesses outstanding electrochemical reversibility. The Ragone plot of symmetric supercapacitor from Figure 4(d) shown that the symmetric supercapacitor based on NHPC-600 electrode exhibits a high energy density of 23.6 $Wh\,kg^{-1}$ at a power density of 500 $W\,kg^{-1}$, and maintain 13.6 $Wh\,kg^{-1}$ at a high power density of 5000 $W\,kg^{-1}$. The maximum energy density symmetric supercapacitor in neutral Na_2SO_4 aqueous electrolyte is much higher than that in alkali KOH aqueous electrolyte (Figure 4d) and is also superior to most of the previously reported carbon-based symmetric supercapacitors in aqueous electrolytes (Table S2).[46–50] Nyquist plots of symmetric supercapacitor is presented in Figure 4(e). A small real axis (Z′) intercept and small semicircle in high
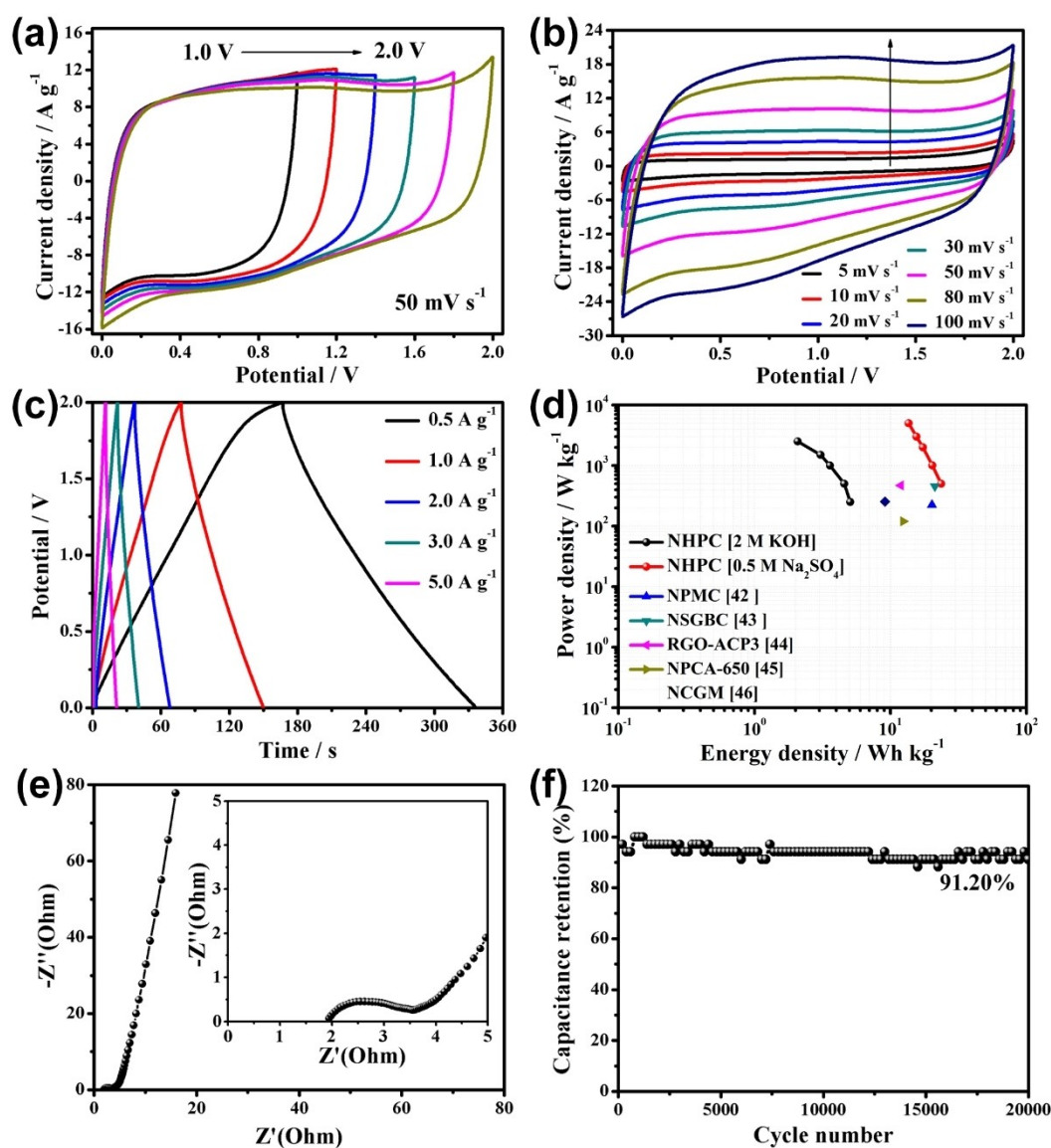

Figure 4. a) CV curves of the aqueous symmetric supercapacitor in 0.5 M Na_2SO_4 electrolyte at different operating voltages; b) CV curves of the symmetric supercapacitor at different scan rates; c) GCD curves of symmetric supercapacitor at different current densities; d) Ragone plot of symmetric supercapacitors; e) Nyquist plot and f) cycling stability of symmetric supercapacitor.

frequency region, and more than 45° sloping curves in low-frequency region are suggested fast electrolyte diffusion rate with low series resistance ($R_s = 0.25\ \Omega$) and low charge transference resistance ($R_{ct} = 1.94\ \Omega$), respectively. The cycle stability of the symmetric supercapacitor was evaluated at a constant current density of $5\ A\,g^{-1}$ with an operating voltage of 2.0 V for 20,000 cycles (Figure 4f). One can see that the symmetric supercapacitor can maintain about 91.2% of the original specific capacitance after 20,000 cycles, indicating its superior long-term lifespan.

Conclusion

To sum up, we demonstrate an integrated activation, catalysis and self-generated template assisted pyrolysis of polyimide strategy to achieve nitrogen self-doped honeycomb-like porous carbon nanoframework (NHPC) with rich planar holes. The experiment results indicate that K_2FeO_4-assisted activation involves potassium and/or iron compounds activation, self-generated metallic compound nanoparticles template and gasification expansion processes, thus promote the formation of honeycomb-like porous carbon nanoframework with planar holes. In addition, the density of planar holes in carbon skeleton can be flexibly controlled by adjusting the carbonization temperature. Based on the integral and interconnected carbon nanoframework structure, abundant and uniform planar holes in carbon skeleton, and high nitrogen doping content to provide fast electron transmission paths and electrolyte ion penetration channels, the NHPC possesses high specific capacitance of $288\ F\,g^{-1}$ at $0.5\ A\,g^{-1}$ and excellent rate capability. Furthermore, a symmetric supercapacitor assembled based on NHPC electrodes display a wide operating voltage of 2.0 V, carries high energy density of high energy density of $23.6\ Wh\,kg^{-1}$ at $500\ W\,kg^{-1}$ and outstanding long-term lifespan with 91.2% capacitance retention after 20,000 charge/discharge cycles. Compared with previously reported methods, the presented fabricate strategy of honeycomb-like porous carbon nanoframework with rich planar holes involved "bottom-up" self-assembly and subsequent self-generated template assisted carbonization is more economical, ingenious and controllable, as well as highly scalable. Moreover, the prepared NHPC materials have high surface area, abundant pore structure and highly controllable planar pores, providing promising candidates for advanced energy storage and conversion.

Experimental Section

Materials

Benzophenone-3,3′4,4′-tetracarboxylic dianhydride (BTDA, 96%) and potassium ferrate (K_2FeO_4, 98%) were purchased from Aladdin reagent, China. Ethylenediamine (EDA, 99%) was purchased from Yantai Chemical Co., Ltd. All other chemicals were commercially analytical grade reagents without further purification.

Synthesis of polyimide (PI) microspheres

Briefly, EDA (0.58 g) and BTDA (3.12 g) were consecutively dissolved in DMF solution (60 mL), and then stirring overnight to obtain a uniform and transparent yellowish viscous polyamic acid (PAA) solution. Subsequently, as-made PAA solution was poured into an autoclave with Teflon-inner to further heated at 180 °C for 10 h. The resulting khaki solid precipitate was collected by centrifugation and repeatedly washed with ethanol and DMF. Ultimately, the product of polyimide (PI) powder was dried under vacuum oven at 60 °C.

Preparation of nitrogen self-doped porous carbon nanoframework (NHPC)

The as-made PI powder (2.0 g) was mixed with K_2FeO_4 (2.0 g) to form a carbon precursor mixture. The carbon precursor was first pre-carbonized at 350 °C for 1 h at a heating rate of $1\ °C\,min^{-1}$ in a quartz furnace tube under flowing N2, followed increased to the ultimate temperatures (500, 600 or 700 °C) for 1 h with a heating rate of $3\ °C\,min^{-1}$. After being cooled to room temperature, the resulting sample was then immersed in 2 M HCl solution and stirred at 90 °C for 12 h to remove the metallic ion, and then the sample was thoroughly washed by distilled water and dried in an oven at 60 °C. The carbon materials obtained at different carbonization temperatures (500, 600, and 700 °C) were labeled as NHPC-500, NHPC-600 and NHPC-700, respectively.

As comparison, the control sample was prepared by directly pyrolysis of PI powder under the same condition of NHPC-600 but without addition of activating agent (K_2FeO_4). The resultant carbon material was labeled as PI-600.

Conflict of Interest

The authors declare no conflict of interest.

Data Availability Statement

The data that support the findings of this study are available from the corresponding author upon reasonable request.

[1] Y. Ge, Z. Shi, C. Tan, Y. Chen, H. Cheng, Q. He, H. Zhang, *Chem* **2020**, *6*, 1237–1253.

[2] M. Jana, R. Xu, X. Cheng, J. S. Yeon, J. M. Park, J. Huang, Q. Zhang, H. S. Park, *Energy Environ. Sci.* **2020**, *13*, 1049–1075.

[3] M. Yu, R. Dong, X. Feng, *J. Am. Chem. Soc.* **2020**, *142*, 12903–12915.

[4] S. Kim, M. Ju, J. Lee, J. Hwang, J. Lee, *J. Am. Chem. Soc.* **2020**, *142*, 9250–9257.

[5] F. Bonaccorso, L. Colombo, G. Yu, M. Stoller, V. Tozzini, A. Ferrari, R. Ruoff, V. Pellegrini, *Science* **2015**, *347*, 1246501.

[6] L. Yao, J. Lin, H. Yang, Q. Wu, D. Wang, X. Li, L. Deng, Z. Zheng, *Nanoscale* **2019**, *11*, 11086–11092.

[7] H. Huang, H. Shi, P. Das, J. Qin, Y. Li, X. Wang, F. Su, P. Wen, S. Li, P. Lu, F. Liu, Y. Li, Y. Zhang, Y. Wang, Z. Wu, H. Cheng, *Adv. Funct. Mater.* **2020**, *30*, 1909035.

[8] Z. Song, L. Miao, L. Ruhlmann, Y. Lv, D. Zhu, L. Li, L. Gan, M. Liu, *Adv. Mater.* **2021**, *33*, 2104148.

[9] V. Nicolosi, M. Chhowalla, M. G. Kanatzidis, M. S. Strano, J. N. Coleman, *Science* **2013**, *340*, 1226419.

[10] S. Wu, K. San Hui, K. N. Hui, J. M. Yun, K. H. Kim, *Chem. Eng. J.* **2017**, *317*, 461–470.

[11] J. H. Jeong, G. W. Lee, Y. H. Kim, Y. J. Choi, K. C. Roh, K. B. Kim, *Chem. Eng. J.* **2019**, *378*, 122126.

[12] C. Hu, L. Gong, Y. Xiao, Y. Yuan, N. M. Bedford, Z. Xia, L. Ma, T. Wu, Y. Lin, J. W. Connell, R. Shahbazian-Yassar, J. Lu, K. Amine, L. Dai, *Adv. Mater.* **2020**, *32*, 1907436.

[13] Y. Zhu, S. Murali, M. Stoller, K. Ganesh, W. Cai, P. Ferreira, A. Pirkle, R. Wallace, K. Cychosz, *Science* **2011**, *332*, 1537–1541.

[14] M. Patel, W. Feng, K. Savaram, M. R. Khoshi, R. Huang, J. Sun, E. Rabie, C. Flach, R. Mendelsohn, E. Garfunkel, *Small* **2015**, *11*, 3358–3368.

[15] Y. He, X. Zhuang, C. Lei, L. Lei, Y. Hou, Y. Mai, X. Feng, *Nano Today* **2019**, *24*, 103–119.

[16] A. C. Lokhande, I. A. Qattan, C. D. Lokhande, S. P. Patole, *J. Mater. Chem. A* **2020**, *8*, 918–977.

[17] Z. Xu, X. Zhuang, C. Yang, J. Cao, Z. Yao, Y. Tang, J. Jiang, D. Wu, X. Feng, *Adv. Mater.* **2016**, *28*, 1981–1987.

[18] C. Li, Q. Li, Y. V. Kaneti, D. Hou, Y. Yamauchi, Y. Mai, *Chem. Soc. Rev.* **2020**, *49*, 4681–4736.

[19] R. Dong, T. Zhang, X. Feng, *Chem. Rev.* **2018**, *118*, 6189–6235.

[20] Z. Li, Z. Lin, *ACS Nano* **2021**, *15*, 3152–3160.

[21] S. Zhao, D. W. Wang, R. Amal, L. Dai, *Adv. Mater.* **2019**, *31*, 1801526.

[22] X. Zheng, L. Miao, Z. Song, W. Du, D. Zhu, Y. Lv, L. Li, L. Gan, M. Liu, *J. Mater. Chem. A* **2022**, *10*, 611–621.

[23] H. Peng, S. Qi, Q. Miao, R. Zhao, Y. Xu, G. Ma, Z. Lei, *J. Power Sources* **2021**, *482*, 228993.

[24] W. Tian, H. Zhang, X. Duan, H. Sun, G. Shao, S. Wang, *Adv. Funct. Mater.* **2020**, *30*, 1909265.

[25] J. Jiang, P. Nie, B. Ding, Y. Zhang, G. Xu, L. Wu, H. Dou, X. Zhang, *J. Mater. Chem. A* **2017**, *5*, 23283–23291.

[26] Y. Gong, D. Li, D. Luo, Q. Fu, C. Pan, *Green Chem.* **2017**, *19*, 4132.

[27] M. Yu, D. Lin, H. Feng, Y. Zeng, Y. Tong, X. Lu, *Angew. Chem. Int. Ed.* **2017**, *56*, 5454–5459; *Angew. Chem.* **2017**, *129*, 5546–5551.

[28] M. Mansuer, L. Miao, D. Zhu, H. Duan, Y. Lv, L. Li, M. Liu, L. Gan, *Mater. Chem. Front.* **2021**, *5*, 3061–3072.

[29] A. G. Shtukenberg, Y. O. Punin, E. Gunn, B. Kahr, *Chem. Rev.* **2012**, *112*, 1805–1838.

[30] L. Machala, R. Zboril, V. K. Sharma, J. Filip, O. Schneeweiss, Z. Homonnay, *J. Phys. Chem. B* **2007**, *111*, 4280–4286.

[31] S. Bhattacharyya, *J. Phys. Chem. C* **2015**, *119*, 1601–1622.

[32] D. Adinata, W. M. A. W. Daud, M. K. Aroua, *Bioresour. Technol.* **2007**, *98*, 145–149.

[33] K. Y. Foo, B. H. Hameed, *Bioresour. Technol.* **2011**, *102*, 9814–9817.

[34] R. Zhang, W. Li, G. Hao, A. Lu, *Nano Res.* **2021**, *14*, 3159–3173.

[35] R. Zhao, H. Peng, H. Wang, J. Liang, Y. Lv, G. Ma, Z. Lei, *J. Energy Storage* **2020**, *28*, 101174.

[36] Z. Song, H. Duan, L. Miao, L. Ruhlmann, Y. Lv, W. Xiong, D. Zhu, L. Li, L. Gan, M. Liu, *Carbon* **2020**, *168*, 499–507.

[37] Y. Wang, R. Liu, Y. Tian, Z. Sun, Z. Huang, X. Wu, B. Li, *Chem. Eng. J.* **2020**, *384*, 123263.

[38] L. Zu, W. Zhang, L. Qu, L. Liu, W. Li, A. Yu, D. Zhao, *Adv. Energy Mater.* **2020**, *10*, 2002152.

[39] B. Manoj, A. G. Kunjomana, *Int. J. Electrochem. Sci.* **2012**, *7*, 31273134.

[40] M. Liu, L. Gan, W. Xiong, Z. Xu, D. Zhu, L. Chen, *J. Mater. Chem. A* **2014**, *2*, 2555–2562.

[41] R. Cai, B. You, M. Chen, L. Wu, *Carbon* **2019**, *150*, 43–51.

[42] L. Sun, C. Tian, Y. Fu, Y. Yang, J. Yin, L. Wang, H. Fu, *Chem. Eur. J.* **2014**, *20*, 564–574.

[43] G. Salitra, A. Soffer, L. Eliad, Y. Cohen, D. Aurbach, *J. Electrochem. Soc.* **2000**, *147*, 2486.

[44] H. Peng, J. Liang, R. Zhao, F. Wang, G. Wei, J. Zhou, G. Ma, Z. Lei, *Electrochim. Acta* **2019**, *300*, 290–298.

[45] G. Zhao, C. Chen, D. Yu, L. Sun, C. Yang, H. Zhang, Y. Sun, F. Besenbacher, M. Yu, *Nano Energy* **2018**, *47*, 547–555.

[46] X. Xin, H. Kang, J. Feng, L. Sui, H. Dong, P. Zhao, B. Pang, Y. Chen, Q. Sun, S. Ma, R. Zhang, L. Dong, L. Yu, *Chem. Eng. J.* **2020**, *393*, 124710.

[47] L. Ji, B. Wang, Y. Yu, N. Wang, J. Zhao, *Electrochim. Acta* **2020**, *331*, 135348.

[48] J. Wang, Q. Li, C. Peng, N. Shu, L. Niu, Y. Zhu, *J. Power Sources* **2020**, *450*, 227611.

[49] P. Li, H. Xie, Y. Liu, J. Wang, X. Wang, Y. Xie, W. Hu, T. Xie, Y. Wang, Y. Zhang, *Electrochim. Acta* **2020**, *353*, 136514.

[50] H. Jia, H. Zhang, S. Wan, J. Sun, X. Xie, L. Sun, *J. Power Sources* **2019**, *433*, 226712.